CONFIDENTIAL. Limited circulation. For review only
IEEE T-RO Submission no.: 20-0411.2

1

An Abdominal Phantom with Tunable Stiffness Nodules and Force Sensing Capability for Palpation Training

Liang He[1], Nicolas Herzig[2], Simon de Lusignan[3], Luca Scimeca[4], Perla Maiolino[5], Fumiya Iida[4], and Thrishantha Nanayakkara[1]

Abstract—Robotic phantoms enable advanced physical examination training before using human patients. In this paper, we present an abdominal phantom for palpation training with controllable stiffness liver nodules that can also sense palpation forces. The coupled sensing and actuation approach is achieved by pneumatic control of positive-granular jammed nodules for tunable stiffness. Soft sensing is done using the variation of internal pressure of the nodules under external forces. This paper makes original contributions to extend the linear region of the neo-Hookean characteristic of the mechanical behavior of the nodules by 140% compared to no-jamming conditions and to propose a method using the organ level controllable nodules as sensors to estimate palpation position and force with a root-mean-square error (RMSE) of 4% and 6.5%, respectively. Compared to conventional soft sensors, the method allows the phantom to sense with no interference to the simulated physiological conditions when providing quantified feedback to trainees, and to enable training following current bare-hand examination protocols without the need to wear data gloves to collect data.

Index Terms—Soft organ simulation, tunable stiffness, soft sensing, abdominal palpation, robotic training phantom.

I. INTRODUCTION

GENERAL practitioners (GPs), along with other clinicians, use abdominal palpation as a key technique in physical examination. During this procedure, a GP palpates the patient's body with their fingers and palms to feel the texture, stiffness, size, form, position, and dullness of the internal organs [1], [2]. Unlike diagnosis that only requires visual or auditory cues, palpation also focuses on haptic information, which is difficult to be trained and requires a considerable amount of time spent on hands-on practice [3]. A good understanding of the palpation technique and organ texture can not only ensure the GP to have accurate diagnosis with manual palpation, but also helps practitioners to interpret other investigation methods such as ultrasonography, computed tomography, and magnetic resonance imaging [4].

Conventional palpation training methods, such as theatre type demonstration, role-play of healthy subjects, static

[1] L. He, and T. Nanayakkara are with Dyson School of Design Engineering, Imperial College London, SW7 2AZ, UK l.he17@imperial.ac.uk
[2] N. Herzig is with School of Engineering and Informatics, University of Sussex, UK
[3] S. de Lusignan is with Nuffield Department of Primary Care Health Sciences, University of Oxford, UK
[4] L. Scimeca and F. Iida are with Department of Engineering, University of Cambridge, UK
[5] P. Maiolino is with Oxford Robotics Institute, University of Oxford, UK

manikins, and engagement with real patients, have the limitations of irregular accessibility, limited conditions, non-repeatability, and insufficient quantified feedback. This poses the need for a robotic abdominal phantom that can simulate a variety of physiological conditions and sense palpation force and position to provide comparative feedback. Such a robotic phantom can also reduce the risk of causing complications on patients due to inexperienced trainees [5]. Medical training simulators are designed with the aim of increasing training efficiency and improving learning outcomes. Currently, major works focus on designing virtual-reality (VR) training systems [6], [7], physical training models for simulation [8], or combining VR or augmented reality (AR) with a physical model in the design [9], [10].

Hyde et al. designed a human-like physical abdominal simulator with pre-casted replaceable diseased liver made of silicone that only simulates limited static symptoms [11]. Inoue et al. used stretchable rubber sheets to simulate different stiffness for the abdomen through variable tension focusing only on the surface, not the organs [12]. Current abdominal simulators do not integrate sensors at the level of physiological abnormalities to monitor how palpation is done around them. By integrating soft sensing into the system, it would not only present realistic training scenarios via haptic feedback but also enable the possibility of the system to include other modalities of feedback related to the sensor readings (visual, vocal, etc.). This type of actuation and sensing builds as the foundation of the robotic replica to ensure multimodal sensory simulation and communication within the human-robot system.

The challenge for such an approach is to design a sensing system that introduces minimum interference to the physiological condition being presented and the GP's bare-hand examination protocol. For instance, most tactile sensor skins may introduce an electronic crust alien to the simulated soft organ [13], and a sensing glove could affect the bare-hand examination protocol the GPs perform.

Currently, tunable stiffness and soft sensing tend to be studied separately in the field of robotics. Tunable stiffness actuation approaches such as granular jamming [14] and layer jamming [15] are suitable for human-interaction due to the high flexibility, wide-stiffness range, and low cost. Magneto-Rheological (MR) fluid [16] and phase-change material [17] have the advantages of physical simulation accuracy but need complex control conditions. Pneumatic inflation, on the other hand, is compact in control and flexible to be integrated

CONFIDENTIAL. Limited circulation. For review only
IEEE T-RO Submission no.: 20-0411.2

2

into diverse systems [18]. However, the elastomeric material is prone to exhibit non-linear deformation when stiffness is controlled [19]. Conventional sensing methods focused on adding additional sensors in the actuation system. With the use of capacitive [20], piezoelectric [21], and piezo-resistive [22] sensors, tactile information can be accurately obtained, but those sensors are difficult to be manufactured as flexible and soft as human tissue. Optical [23], magnetic [24], carbon nanotubes [25], conductive liquids [26], and conductive polymers [27] sensors show good flexibility, but the electronics and specific fabrication process make it difficult to be embedded in soft phantom with complex geometry.

Adding an additional soft sensing system to the tunable stiffness design not only requires additional hardware but also could affect the simulated physiological conditions. In addition, only having the force information at the surface level would limit the potential of the simulator as it is more important to understand how the patient feels at the organ level during the palpation according to the palpation protocol [3]. These difficulties reveal a gap for an integrated soft actuation and sensing technique for abdominal simulator designs that required both presenting various organ abnormalities and monitoring palpation force and its location for multimodal feedback such as location and force-dependent visual feedback.

Thus, we explored the sensing capability of the existing fluid-based actuation system instead of adding additional sensors to the tunable-stiffness organ design. Building on the advanced development of the pneumatic deformation [28] and hydraulic [29] pressure sensing, the tunable stiffness effect of granular jamming was studied. We combined the sensing and actuation techniques in such a pneumatic approach and designed a dual-functional soft nodule that couples tunable stiffness and soft sensing with a single control system.

The nodule actuator/sensor is made of two layers of rubber membrane with ground coffee in between. When the internal layer is inflated, the ground coffee will form a hard crust with "craggy" surface due to the effect of granular jamming [30]. When an external force is applied to the nodule, the internal pressure will change in regard to the applied force. In [30], we presented a controllable organ design with granular jamming based nodules for stiffness changing, focusing on the liver design with the physiological consideration in size, weight, stiffness, texture, and appearance. In this paper, we deeply characterized the stiffness control of the single nodule and further explored its inherent sensing capabilities by comparing the granular jamming state and the no-jamming state. Results validate the hypothesis that the granular jamming effect can help to extend the linear region of the Neo-Hookean mechanical behavior of pure rubber membranes (by 140% of the no-jamming condition).

Such actuators/sensors were experimentally supported and tested using an abdominal phantom consisting of a soft robotic liver with multiple nodules. Each nodule can be controlled and tuned to a range of stiffness, and therefore, can dynamically simulate a number of diseased liver conditions. Individual nodules can be used as force sensors for specific target tumors of the liver. A methodology to generalize the multi-nodule
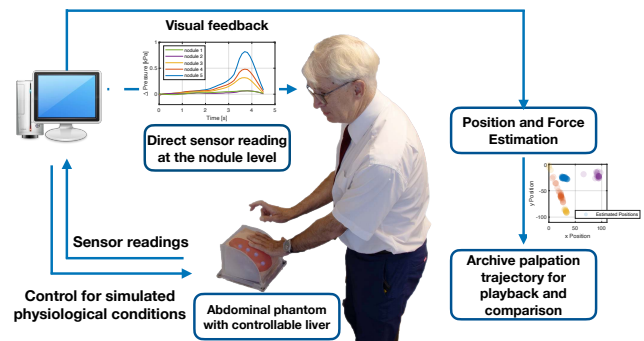

Fig. 1: Possible training scenarios with the abdominal phantom with soft robotic liver. Haptic feedback of diverse liver conditions can be simulated through the phantom control. Meanwhile, the embedded soft sensor readings of the dual-functional system allow the possible representation of other modalities of feedback during palpation, such as patient facial expression, vocal feedback. One example type of visual feedback that indicates pressures applied to individual nodules is shown in the figure. The system enabled the closed-loop information cycle for the training as the trainee regulates their action based on the provided multimodal feedbacks similar to the doctor communicate to the patient during practical palpation. In addition, the palpation force and trajectory can also be recorded during the training for playback, comparison, and further studies.

sensing approach in soft materials with complex geometry was also presented to show the estimation of palpation position and force.

The physiological concerns and motivations are described in Section II. Section III gives the details of the design and manufacturing procedure for the nodules and the abdominal phantom. Section IV discusses the experimental characterization of stiffness tuning and sensing capability of a single nodule. A demonstration of the robotic abdominal phantom with multiple nodules is tested and analyzed in Section V with a proposed methodology to obtain the generalized model via sensor pre-characterization. Potential applications and future works are discussed in depth in Section VI.

II. PHYSIOLOGICAL DESIGN OBJECTIVES AND POSSIBLE TRAINING SCENARIOS

The liver is usually the first palpation site in a typical abdominal examination procedure. In [30], we studied the size and shape of the liver and characterized the material properties for the design of controllable liver phantom (the weight of the liver is around 1200g; the length of the liver span was 16cm; the height of the liver span was 10cm; the normal liver texture were designed to be smooth without any irregularities [3]). The same design parameters and material properties were used in this study. Most parts of the liver are concealed by the right rib cage and difficult to be felt by the GPs. However, in diseased conditions such as fatty infiltration, active hepatitis, cirrhosis, and hepatic neoplasm, the abnormality can be physically detected through physical

CONFIDENTIAL. Limited circulation. For review only
IEEE T-RO Submission no.: 20-0411.2

3

examination of the lower edge of the liver [31]. The physical simulations in our design were, therefore, focused on the lower part of the liver and the liver edge. Liver tumor stiffness varies according to tumor pathology. In this paper, we demonstrate the physical simulation of T1 and T2 stage tumors (according to the TNM classification) via two types of tunable spherical nodules with an assumption that early-stage tumors can be modeled as spherical incursion [32], [33]. With the measurement of transient elastography, data shows the stiffness of liver tumors is between 16.9 kPa and 75 kPa [34]. The above stiffness range was used as the reference for the tumor stiffness simulation in our study. By changing the design of the size and positions of the nodules, T3 tumors can also be simulated with the same methodology.

According to the physical examination protocol, physicians make the diagnosis by associating their exteroceptive tactile sensation with proprioception of their palpation motions and information gained via other types of sensations (such as visual from patient facial expression and vocal communications with the patient [1]). With training tasks through static manikins, it is difficult for the trainee to learn such a multimodal information integration. An abdominal phantom with coupled actuation and sensing provides the potential to allow training with integrated multiple sensations. In the programmed training scenarios, high-fidelity physical haptic features can be simulated with interaction data recorded to present simulations of additional modalities. In Fig. 1, an example of visual feedback of the pressure applied to individual tumors was presented to allow the trainee to practice visual/haptic dual-modality sensation during the training. The trainee can, therefore, regulate their motions to gain maximum information about the mechanical properties of the organ while keeping the stress on the organ to a minimum. With such a sensorized system, palpation data such as the palpation trajectory and force distribution of the trainees and experts are also archivable for playback and comparison.

III. Design of the Abdominal Phantom

In this section, the design and fabrication of the single positive granular jamming nodule and the proposed abdominal phantom are presented and discussed. Each positive granular jamming nodule couples the function of actuation (tunable stiffness) and sensing.

It is known that rubber under certain conditions exhibits neo-Hookean behavior [35]. Experimental data also shows a rubber balloon experiences an initial linear stage where the internal pressure increases with the circumferential stretch [36]. After the pressure reaches its maximum, the rubber balloon will expand suddenly with a drop of pressure. This dynamic character caused by the deformation dependent pressure load is known as snap buckling [37]. Thus, to use such a pressurized nodule as a soft actuator/sensor, the range of the linear pressure controlled region of the dual-functional soft nodule in the liver phantom is a key design criterion. We predict that positive pressure granular jamming will help to extend the linear region of the neo-Hookean behavior of the rubber balloon in pressure control. Ground coffee has been chosen in the
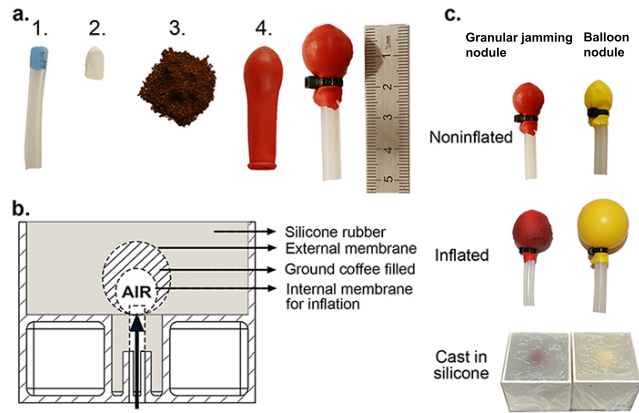

Fig. 2: **(a)** The process of making the single positive granular jamming nodule. 1. silicone tube with reinforcement, 2. inner layer rubber membrane, 3. 1.5g ground coffee, 4. external rubber membrane. **(b)** Structure of the single nodule silicone sample with ground coffee. **(c)** Comparison between the sample with a granular jamming nodule and the sample with balloon nodule (both were pressurized around 110 kPa).
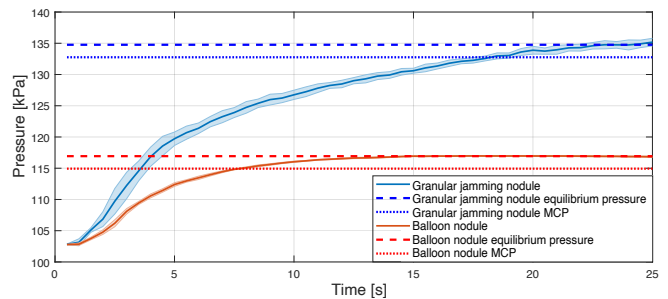

Fig. 3: Internal pressure change of the single nodules after casting in silicone. The pressure reaches equilibrium at around 134.7 kPa and 116.9 kPa for samples with positive granular jamming nodule and samples with balloon nodule, respectively. Maximum control pressure (MCP) was defined as 2 kPa less than the measured equilibrium pressure; The mean value and the standard deviation errors (indicated by the shaded area) of the 21 trials of experiments show good repeatability of both samples during the inflation.

study for providing positive granular jamming due to its high strength-to-weight ratio, stiffness-to-density, and yield stress [38]. Ground coffee also exhibits stress-strain response of an elastic regime followed by a plateau regime under compression test [38], which is suitable for our application in tunable-stiffness.

A. Design of the Single Nodule

The positive granular jamming nodule was created by combining two layers of rubber membrane with 1.5 g ground coffee in between (see Fig. 2a). The inner membrane is 5 mm in diameter and 10 mm in length. The external membrane has a spherical shape with a diameter of 15 mm. A flexible silicone tube with an outer diameter of 6.4 mm (bore size

CONFIDENTIAL. Limited circulation. For review only
IEEE T-RO Submission no.: 20-0411.2

4

3.2 mm) was used as the air channel for the pneumatic operation. By inserting a section of polyamide tube (1025P series, Parker Legris) 4 mm in diameter and 5 mm in length inside the silicone tube, the membranes were fixed and made airtight by cable ties. The silicone tube has a good sealing property in pneumatic connection while it is flexible enough to make air channels in the model. A single nodule with only two layers of membranes was also created for comparison. Fig. 2c shows the two types of nodules in deflated and inflated states, respectively. The nodule with positive granular jamming effect formed a spherical crust with "craggy" surface, while the nodule without ground coffee inflated to a larger size with a smooth surface at the same pressure condition. The two nodules were then cast in silicone rubber (Smooth-on Ecoflex 00-10 with part A, part B, and Slacker maxing ratio of 1:1:2) for studying their performance in a physically simulated in-organ environment. Both samples were embedded at 5 mm depth from the surface in the in 3D printed boxes ($60 \times 60 \times 30$mm; ABS plastic; designed to fix the nodule with increased robustness), see Figs. 2b. Fig. 3 shows the internal pressure change of the two single nodule samples during continuous inflation with a constant pumping flow rate of 2L/min. 21 trials of data were collected for each sample. The internal pressure of the samples first increases rapidly, then maintains steady at a certain pressure, which we name to be the equilibrium pressure in this paper. The equilibrium pressures of the two samples were measured as the point where the increase of pressure was less than 0.05 kPa per second during the continuous constant flow rate inflation. The threshold 0.05 kPa/s is defined based on the noise of the signal (around 0.1 KPa under 1k Hz sampling rate) and the closed-loop pressure controller performance (see section. III-C). From Fig. 3, we can notice that sample with positive granular jamming nodule reaches the equilibrium pressure at approximately 134.7 kPa, while sample with balloon nodule reaches the equilibrium pressure at a lower pressure condition (around 116.9 kPa).

According to the ideal gas law, $PV = nRT$ (where, P, V, and T are the pressure, volume, and absolute temperature, n, R are the number of moles of gas and the ideal gas constant, respectively), if the internal pressure P remains steady, the nodule size V will continue to increase when air n is pumped in. Significant size increases were observed after the samples reached their equilibrium pressures. The pressure-based control also becomes invalid when the internal pressure reaches the equilibrium pressure. Thus, a maximum control pressure (MCP) was defined as 2 kPa less than the measured equilibrium pressure (sample with granular jamming nodule $MCP = 132.7$; sample with balloon nodule $MCP = 114.9$). The valid pressure-based control region is defined as from the atmospheric pressure to the MCP.

B. Design and Fabrication of the Abdominal Phantom

The prototyping of the abdominal phantom simulator consists of soft robotic liver fabrication, abdominal phantom casting, pneumatic actuation, and sensing electronics. Due to the natural geometry of the human liver and the importance of liver edge in palpation, the four granular jamming nodules
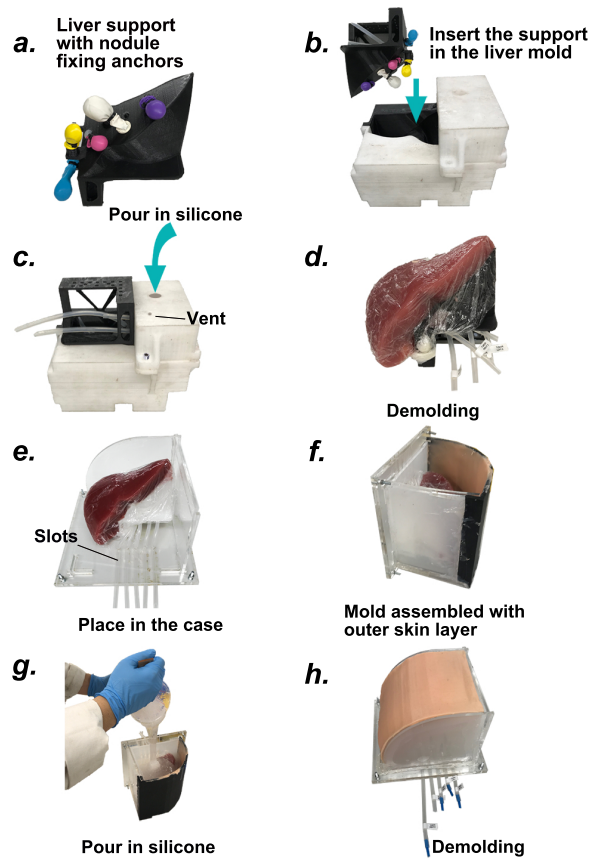

Fig. 4: Layered fabrication process of the abdominal phantom with liver nodules providing coupled force sensing and tunable stiffness actuation. **(a)** Place the pre-made nodules on the support structure by the fixing anchors. **(b)** Insert the support in the liver mold. Fasten the mold with nuts and bolts and seal it with a hot glue gun. **(c)** Pour in pre-mixed silicone slowly (Ecoflex 00-10 part A, part B, and Slacker with a mixing ratio of 1:1:2). The silicone mixing ratio was chosen due to the close stiffness to ex-vivo porcine liver [30]. **(d)** Remove the liver from the mold carefully and wrap it with cling film. **(e)** Fix the liver in the laser-cut transparent acrylic case and make sure the silicone tubes go through the slots. **(f)** Prepare the skin layer (3 mm thick; Smooth-on Ecoflex 00-30; skin color pigment added) on a separate mold. Remove the inner layer of the mold and assemble it with the acrylic case. **(g)** Pour in Ecoflex 00-30 to create 3 mm wall on each side of the acrylic case first and then pour in Ecoflex Gel with Slacker (Ecoflex Gel part A, part B, and Slacker with a mixing ratio of 1:1:2) to fill the abdominal cavity with a very soft jelly-like material. **(h)** Demold the out skin layer mold and apply baby powder (Johnson and Johnson) to ensure a non-stick surface.

are designed to be placed at the lower-left lobe surface, the edge of the left lobe, lower-right lobe surface, and lower-right lobe edge for physical tumor simulations. One balloon nodule is placed on the bottom of the right lobe of the liver support structure for representing smooth-surfaced right lobe liver enlargement. The proposed layered fabrication process is described in Fig. 4 a-h.
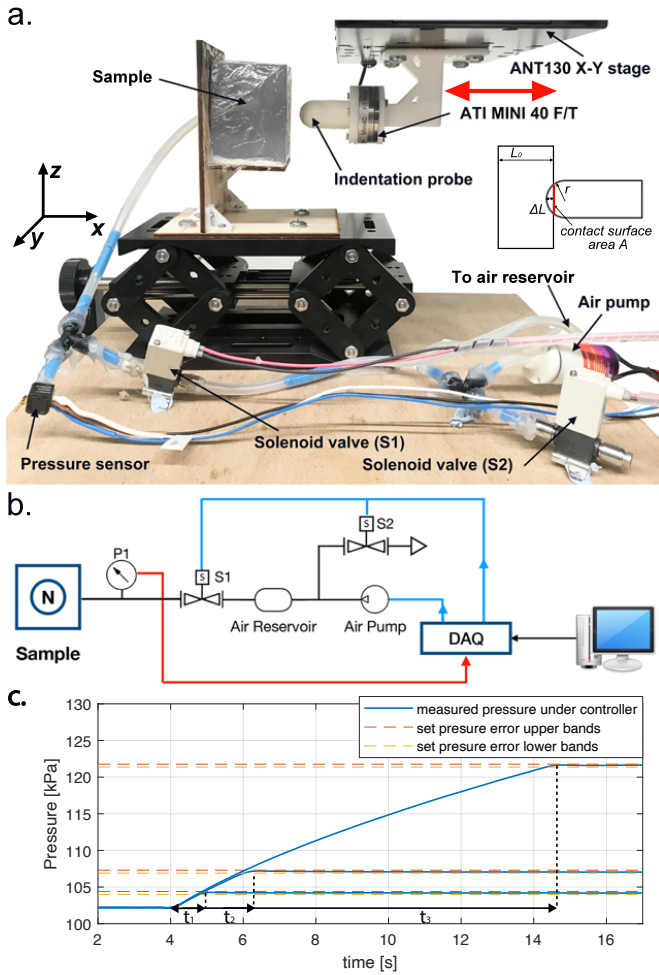
CONFIDENTIAL. Limited circulation. For review only
IEEE T-RO Submission no.: 20-0411.2

5

a.

b.

c.

Fig. 5: **(a)** Indentation experiment set-up for signal nodule samples. **(b)** Connection diagram of the set-up (P1 stands for pressure sensor 1; S1 and S2 stand for solenoid valve 1 and 2; N stands for the nodule cast in the sample). **(c)** Pressure convergence of the controller to set pressures (104, 107, and 121.5 kPa). The error band for set pressures are within 0.4 kPa. t_1, t_2, and t_3 are the time took for converging to the set pressures with the controller.

C. Pressure Control

A closed-loop pressure controller was designed in order to control the internal pneumatic pressure of the nodule. A proportional controller is used to increase the pressure while the computer-controlled valve opening is used to decrease the pressure. An air reservoir is added to stabilize the internal pressure without overshoot. The proportional controller adapts the flow rate of the air pump and the valve opening in order to reach a desired pressure in the nodule. Fig. 5c shows the convergence of the internal pressure of the nodule to the desired set pressure value due to the controller action. The controller was only used when the driving pressure is less than the MCP.

IV. SINGLE NODULE CHARACTERIZATION

To characterize how positive granular jamming nodules show different properties from nodules with only membranes after embedding them in silicone, the indentation test was performed on the two types of samples: sample with granular jamming nodule and sample with balloon nodule (Figs. 2b and 2c). It is well known that the initial stress-strain curve of rubbers determined from the first deformation is unique and cannot be reproduced. According to the Mullins effect, the stress-strain curve of the rubber membrane would approach a steady-state through further repeated inflation [39]. The steady-state stress-strain curves after the repeated inflation treatment will also show little hysteresis at lower strains. In our experiments, all rubber membranes were inflated 10 times to reach the steady-state of the stress-strain behavior before the sample making to ensure repeated performance [40]. The rubber membranes also show a small standard deviation of pressure during inflation across trials after the treatment, as reported in Fig. 3.

A. Methodology and Experiment

Fig. 5 (a) shows the indentation experiment set-up. A 3D printed spherical-tipped probe with a length of 30 mm and a tip diameter of 20 mm was mounted on an ANT130 XY-stage (Aerotech Inc., accuracy of 2.5 μm) to perform the indentation test. The probe dimension was designed similar to the size of a human finger with a spherical tip for safe interaction with the silicone samples. The position and velocity data of the XY-stage were acquired at the frequency of 20 Hz. Additionally, with an ATI Mini40-E Force/Torque sensor (SI-40-2, ATI Industrial Automation, USA, resolution of 0.02 N), force data was collected through a National Instruments data acquisition board (PCIe-6320) during the test. Meanwhile, the sample was connected with a gauge pressure sensor ($0 - 100$ PSI,40PC100G2A, Honeywell), two solenoid valves (S1, S2, VDW10AA, SMC), an air reservoir (rigid plastic, with the volume of 250 ml), and an air pump (SIMILK, mini air pump, rated airflow of 2L/min) during the experiment for pressure control. A National Instrument DAQ (USB-6341) with Labview 2018 was used to acquire the signals and control the experiment. The pneumatic diagram is shown in Fig. 5 (b). The air pump was used for inflating the internal membrane of the samples. Solenoid valve S1 was used for maintaining the internal air mass, while solenoid valve S2 can release the air of the air reservoir through connecting to the environment (atmospheric pressure).

During the experiment, the nodule was first inflated and maintained at a certain driving pressure, followed by the closing of solenoid valve S1. The pressure controller was turned off after the internal pressure of the nodule reached its MCP. The nodule was continually inflated to test the performance after it reaches the equilibrium pressure, with time steps of 0.5s and a constant rated airflow of 2L/min of the pump. The probe then performs the indentation on the sample from the depth of 4 mm to 10 mm with the step of 1 mm. The gauge pressure sensor recorded the internal pressure change during indentation with S1 closed. Based on the amount of
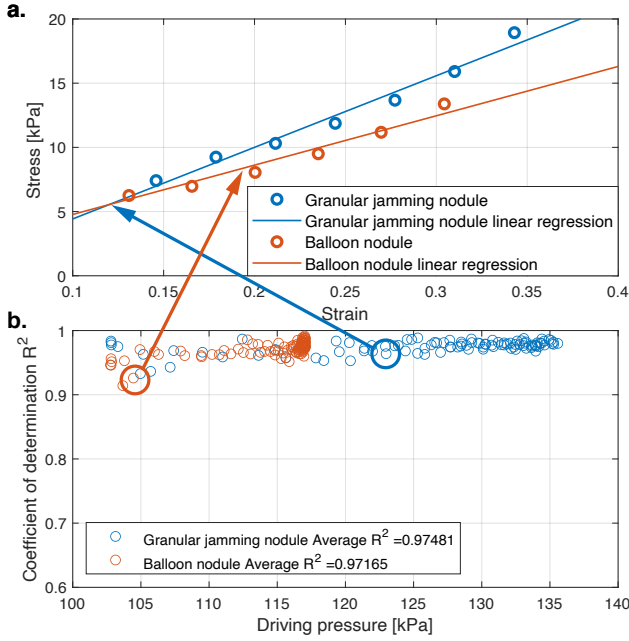
CONFIDENTIAL. Limited circulation. For review only
IEEE T-RO Submission no.: 20-0411.2

6

a.

b.

Fig. 6: **(a)** Example linear regressions of stress and strain at a driving pressure of 123.88 kPa for the sample with granular jamming nodule and 103.79 kPa for the sample with balloon nodule. **(b)** The coefficient of determination R^2 for the linear regression of stress and strain for samples at different driving pressures.

infilled air and different driving pressure conditions, 3 trials of experiments were performed on each sample.

With the indentation tests performed at different driving pressure conditions, the nodule stiffness, size changing, and sensing capability were evaluated separately. Stiffness was calculated as Young's modulus based on the applied force (measured by the Force/Torque sensor) and displacement (measured by the XY-stage). The size-changing were measured by the XY-stage. Results are discussed in Section IV-B. The nodule sensing capability at different pressure conditions was measured by the applied force (measured by the Force/Torque sensor) and related internal pressure change (measured by the gauge pressure sensor), shown in Section IV-C.

B. Nodule stiffness change

The indentation tests provided a method to analyze how the stiffness of the phantom and the volume of the nodules change in regard to the increase of nodule driving pressure. The stiffness of the original silicone without any nodule (Ecoflex 00-10 part A, part B, and Slacker with a mixing ratio of 1:1:2, thickness 30 mm, stiffness $E = 38.7$ kPa) is indicated by a flat line in Fig. 7.

Neo-Hookean model was used to describe the stress-strain curve of the material in this study. In the small strain regime (less than 0.4), we performed a linear approximation of the stress and strain relation to determine the material stiffness.

With the stress and the strain of 7 indentation steps at each pressure condition, linear regression was applied to calculate
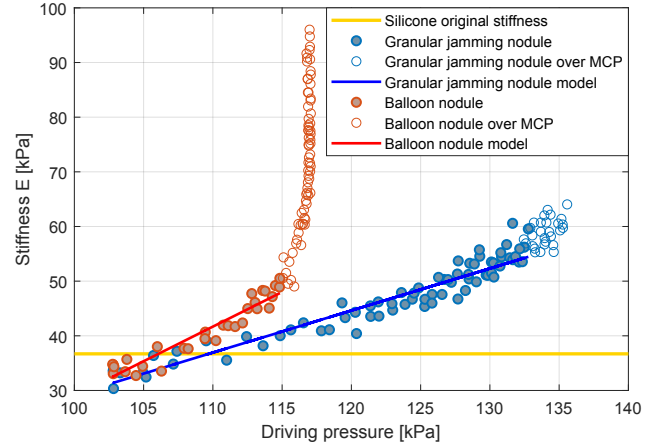

Fig. 7: During inflation, the samples show different stiffness at different pressure. The figure describes the change of material stiffness E [kPa] with the increase of driving pressure during inflation for sample with granular jamming nodule and balloon nodule. The stiffness E was calculated based on the linear regression of the stress and strains as shown in Fig. 6

the stiffness E of the phantom.

$$E = \frac{\sigma}{\epsilon} = \frac{F(L_0 + L_{sz})}{A(\Delta L)} \qquad (1)$$

where, E is the stiffness of the phantom, σ is the stress, ϵ is the strain, F is the mean steady force measurement of a 1-second steady force response after the material relaxation of the peak force response, A is the contact area between the probe and the sample (illustrated in Fig. 5a), L_0 is the initial thickness of the sample, ΔL is the measured indentation depth, and L_{sz} is the measured peak surface deformation of the phantom along the x-direction. The mean of steady force response of each indentation was chosen instead of peak value with the consideration that manual palpation is based on low-frequency movement [3], [41].

The coefficient of determination R^2 of the linear regression at different driving pressures is shown in Fig. 6b. From the figure, we can observe that in general the stress-strain curves of the samples have good linear fits with $R^2 > 0.95$. This implies that nodules can be treated as Hookean objects for the given pressure conditions. The Hookean assumption helps to simplify the modeling for stiffness control with pressure conditions up to their MCP. Example stress-strain linear regressions at a driving pressure of 123.9 kPa for granular jamming nodule and 103.8 kPa for balloon nodule are shown in Fig. 6a. Fig. 7 shows that the internal pressure becomes saturated when the internal pressure approaches the equilibrium pressure. Thus, the model for pressure-stiffness control is limited from atmosphere pressure to the MCP of the sample. An extension of the pressure control region can be clearly observed with the positive granular jamming effect compared to nodules with only rubber membranes. We fitted a linear model for the pressure-stiffness relation of the granular jamming nodule and the balloon nodule. The model is shown

CONFIDENTIAL. Limited circulation. For review only
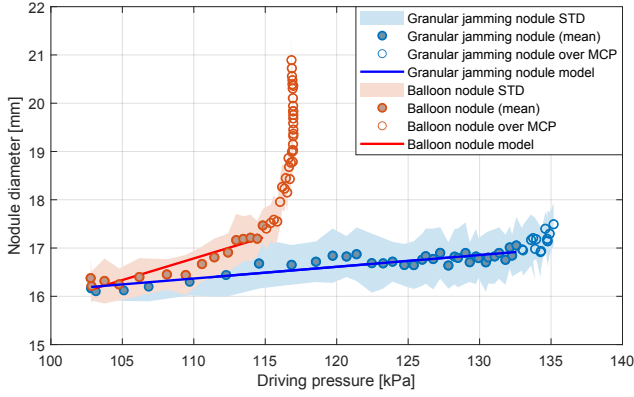IEEE T-RO Submission no.: 20-0411.2

7

Fig. 8: The size change of the nodules during inflation. 21 trials of data were tested for each pressure condition. The mean value and the standard deviation errors of the 21 trials were shown in the figure.

as follow:

$$E_A = 0.77P - 47.7 \tag{2}$$

$$E_B = 1.27P - 97.7 \tag{3}$$

where, E_A and E_B are the stiffness of the granular jamming nodule, and the balloon nodule at pressure P (P is from atmosphere pressure to the MCP). The R^2 of the linear fit for the sample of granular jamming nodule and balloon nodule are 0.92 and 0.89, respectively.

The samples also exhibit a volume change during inflation besides the increase of stiffness. The samples are cast in a box structure (see methods in section III-A and Fig. 2) and only have the capability to change size in the x-direction. We assume the nodules maintain spherical shape during initial inflation with low strain conditions [40]. Considering the incompressibility of the silicone material, the change of the nodule diameter was measured as the center of the silicone surface change along the x-axis (Fig. 5a). The surface position of the sample is calculated as the position of the first contact point of the probe by aligning the force data and probe position data. 21 trials of data were used for determining the nodule size at each pressure condition for each type of sample. The diameter change of the nodules in regard to pressure change is shown in Fig. 8. The original nodule diameter is being considered as the reference 16 mm in the figure. The repeatability of both of the samples under pressure control, represented by the standard deviation data in Fig. 8, are suitable for our application.

In order to better describe the correlation and estimate the nodule size with different driving pressures, we also fitted a linear model for the sample with a granular jamming nodule and the sample with a balloon nodule for the valid pressure control region. The model is as follows:

$$D_A = 0.024P - 2.3 \tag{4}$$

$$D_B = 0.089P - 9.1 \tag{5}$$

where, D_A and D_B are the diameter change of the granular jamming nodule, and the balloon nodule at pressure P (P
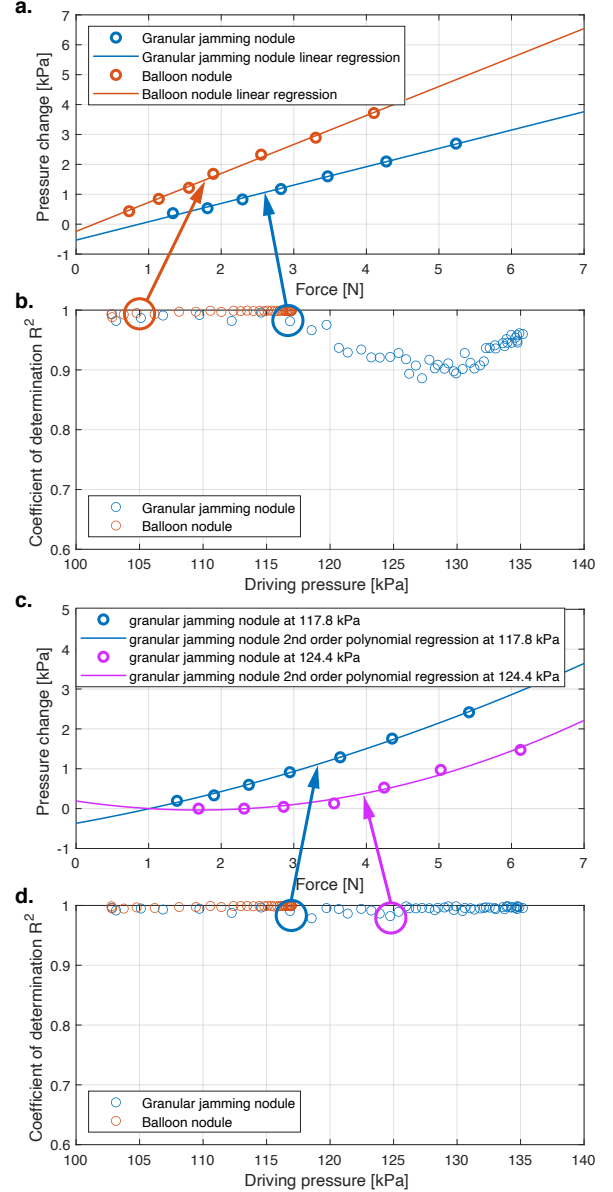

Fig. 9: **(a)** Example linear regressions of pressure change and applied force at driving pressure of 115.6 kPa for the sample with granular jamming nodule and 103.8 kPa for the sample with balloon nodule. **(c)** Example 2nd order polynomial regressions of pressure change and applied force at a driving pressure of 117.8 kPa and 124.4 kPa for the sample with granular jamming nodule. **(b) (d)** The coefficient of determination R^2 for the linear and the 2nd order polynomial regression of pressure change and applied force for samples at different driving pressure conditions, reported as the mean value of 3 trials.

is from atmosphere pressure to the MCP). The R^2 of the linear fit for the sample of granular jamming nodule and balloon nodule are 0.87 and 0.75, respectively. The experiment shows that positive pressure granular jamming nodules exhibit a much lower expansion rate in size compared to nodules with only rubber membranes under the same pressure. Balloon

CONFIDENTIAL. Limited circulation. For review only
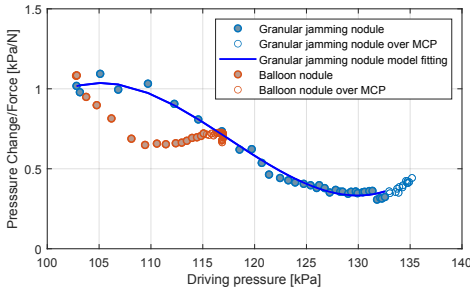IEEE T-RO Submission no.: 20-0411.2

8

Fig. 10: Sensitivity (change of internal pressure per unit external force) for different driving pressure conditions. The sensitivity of each driving pressure condition was calculated based on the linear approximation shown in Fig. 9

nodule presents increased stiffness coupled with significant deformation during inflation due to the material elasticity. The granular jamming effect, on the other hand, compensates the deformation with the increased jamming of the granular particles. This can be used for applications where only tunable stiffness is needed with a small change in deformation. The gradually increased granular jamming effect also acts as an additional constrain to the soft nodule, which flattens the sudden deformation when the internal driving pressure approaches the equilibrium. The positive granular jamming effect can not only simulate a similar texture to tumors [1], [3] but also can simulate a wider linear range of stiffness in pressure compared to nodules with only rubber membranes within the valid pressure-based control regime. The result of 140% of extended pressure-based control regime validates the prediction that positive pressure granular jamming helps to extend the linear region of the neo-Hookean characteristic of the mechanical behavior of the nodule compared to no-jamming conditions. The results can also be used for estimating nodule stiffness during the physical tumor simulation.

C. Nodule sensing capability

The previous section shows that the nodule embedded in silicone can be used to simulate fibrosis in soft tissue with tunable stiffness. During the fibrosis physical simulation process, the nodule also serves as an embedded soft sensor with fluid pressure variations. At this stage, the solenoid valve (S1) was closed, and the pressure was not regulated during the sensing period. When an external force is applied to the nodule, the internal pressure changes can be used to measure the exerted force.

A linear model was first used to study the relation between the pressure and applied force within our compression test range (strain less than 0.4). Regression fits were applied to each set of data (pressure change against applied force) at each selected driving pressure condition. 3 times experiments were done for each driving pressure, and the average data were used for the regression. The experiment set-up was described in Section IV-A. Fig. 9b shows the coefficient of determination R^2 of the linear fit for different driving pressure conditions (an average $R^2 = 0.94$ for sample with granular jamming nodule

and an average $R^2 = 0.99$ for sample with balloon nodule). Fig. 9a shows the example linear regressions at 115.6 kPa for granular jamming nodule and 103.8 kPa for balloon nodule. The linear model allows us to better interpret how the overall sensitivity changed across all valid driving pressures. When the driving pressure is above 120 kPa, a drop of linearity of the sensor can be observed when it approaches the equilibrium pressure for the sample with granular jamming nodules. A 2nd order polynomial fit was also tested to evaluate the nodules, as shown in Fig. 9d. Although the 2nd order polynomial models show better fit for determining local sensitivity of the nodules at all given driving pressures, the 2nd order coefficient (a median of 0.01) is nearly 0 and very small compared to the 1st order coefficient (a median of 0.62). This shows the feasibility of using the linear assumption to evaluate the overall sensitivity changes across different driving pressures. The gradient analysis also allows us to understand how the overall sensitivity changes with different driving pressures.

Based on the linear approximation between the pressure change and applied force, slope K was defined as the sensitivity of the nodules with the unit of [kPa/N]. Fig. 10 shows the relation between the sensitivity and the driving pressure of the nodules with the mean value of 3 trials. The relations were fitted with third-order polynomial models based on Akaike's Information Criterion (AIC) [42] as:

$$S_A = 0.06342P^3 + 0.1203P^2 - 0.2993P + 0.4633 \qquad (6)$$
$$S_B = -0.01395P^3 + 0.1115P^2 - 0.07702P + 0.6632 \quad (7)$$

where, S_A and S_B are the sensitivity of pressure change to applied force for the granular jamming nodule and the balloon nodule at pressure P (where P is normalized by mean 123.1 and std 8.814 for S_A, and mean 109.5 and std 4.404 for S_B).

The results show that both types of nodules exhibit higher sensitivity at lower driving pressure conditions when they are at their softest states. The sensitivity decreases as the internal pressure approach the equilibrium pressure with the linear assumption. The characterized model can be used in estimating the changes of sensitivity with different driving pressure in a broader system with more complex geometry, shown in Section V.

V. EVALUATION ON MULTIPLE-NODULE PHANTOM WITH COMPLEX ORGAN GEOMETRY

The singular nodule design shows the dual-function of tunable stiffness and soft sensing in fibrosis physical simulation. By embedding multiple nodules in the soft organ design, it is possible not only to simulate different tumor locations but also to sense the indentation force and positions through multiple sensor readings. The following section first described the methodology and experiment used for characterizing the multiple nodule phantom sensing properties. With the help of previously characterized signal nodule sensitivity, machine learning tools were used to generalize the model to be able to estimate the palpation force and position even with complex geometry and dynamic driving pressures. Then, we discuss the result of the point-by-point palpation and palpation with different complex motions from direct sensor readings. Finally,

CONFIDENTIAL. Limited circulation. For review only
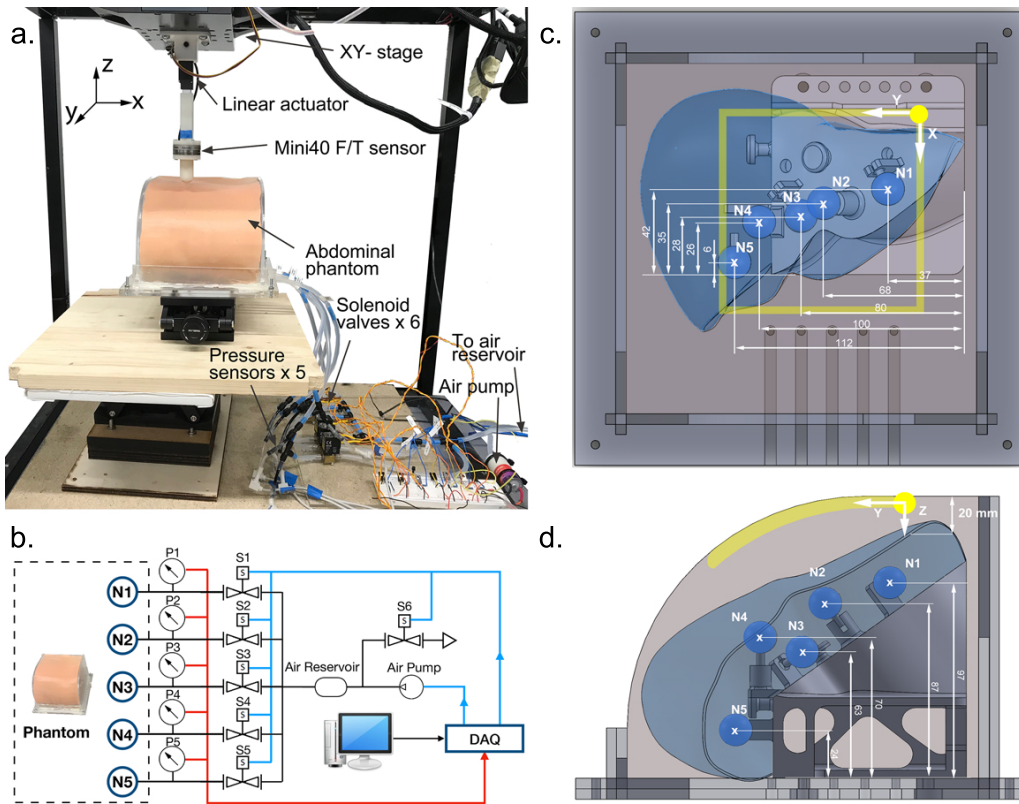IEEE T-RO Submission no.: 20-0411.2

9

Fig. 11: **(a)** Multiple nodule abdominal phantom calibration experiment set-up. **(b)** Connection diagram with nodules N1, N2, N3, N4, N5 embedded in the phantom. **(c)** Top view of the abdominal phantom. The yellow square indicates the area $(100mm \times 100mm)$ used for indentation in the multiple nodule calibration experiments. **(d)** Side view of the abdominal phantom. The shaded yellow line shows the trajectory of the indentations. Positions of the nodules are shown in **(c)** and **(d)**, and all dimensions are in [mm].

we validated and tested the model with multi-axis palpation performed with a robotic arm.

A. Methodology and experiment for calibration

The approach for the calibration of the sensing model of the multi-nodule phantom with embedded liver followed three steps:

1) Point-by-point calibration to generate ground truth location and force data of indentation for selected driving internal pressure of each nodule.
2) With assumption 1: the nodules do not interfere with the sensing model of each other with the currently distributed distance during the indentation; and assumption 2: the nodules follow the same sensitivity curvature as previously characterized signal nodule models (same nodule design, membrane material, and silicone material were used), an enlarged set of training data that covers the entire range of driving pressures combinations of the nodules can be simulated based on the calibrated ground truth data in step 1 and the sensitivity models in Eq. (6) and (7).
3) The experimental calibration training data from step 1 and the simulated training data from step 2 were then combined and shuffled to train a neural network to be

used as a generalized sensing model. The generalized sensing model allows the multiple-nodule abdominal phantom to estimate force and position of palpation even with pressurized conditions (corresponds to the inflating pressures of the nodules) that never been experimentally calibrated.

Fig. 11a shows the experiment set up for the calibration. The abdominal phantom was placed underneath an XY-stage, where a 3D printed probe (diameter of 20 mm) is attached with an ATI Mini40-E Force/Torque sensor to an L16-P Miniature Linear Actuator (Actuonix Motion Devices Inc., Canada) for the indentation. The abdominal phantom was connected with 5 pressure sensors ($\pm100kPa$, PSE 543-R06, SMC Corporation, Japan), 6 solenoid valves (Z031C, Sirai, Italy), one air reservoir (rigid plastic, with the volume of 250 ml), and an air pump (SIMILK, mini air pump, rated airflow of 2L/min). The pressure sensors used in the multiple nodule experiment are from a different manufacturer as the single nodule characterization experiment due to availability. However, both of the sensors give the required accuracy and sensing range for the application. The driving pressures and sensing range in the experiment were expected to be less than +50 Kpa relative to atmospheric pressure. The control and measurement of the experiment were achieved with a National

CONFIDENTIAL. Limited circulation. For review only
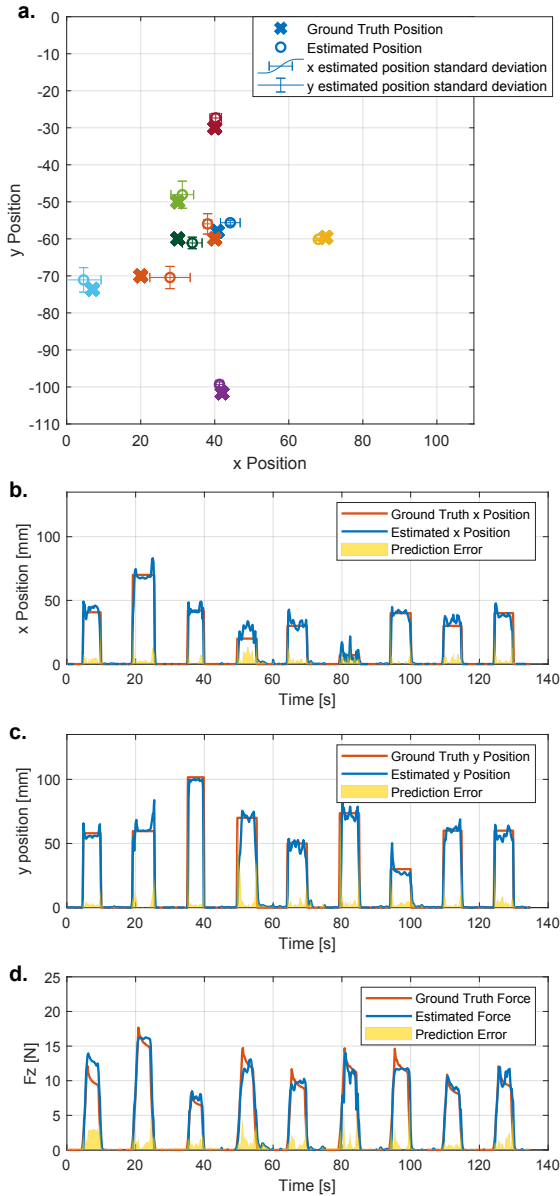IEEE T-RO Submission no.: 20-0411.2

10

Fig. 12: Test with a new indentation experiment with randomly selected driving pressure combinations. **(a)** Ground truth testing indentation positions and the estimated indentation positions with the trained neural network. Standard deviations are shown as the error bars for x and y positions. The data when the robot was not being palpated were excluded. **(b)** Ground truth testing indentation x positions and the estimated x positions. **(c)** Ground truth testing indentation y positions and the estimated y positions. **(d)** Ground truth testing indentation force and the estimated force. Prediction errors are shown with shading in b, c, and d.
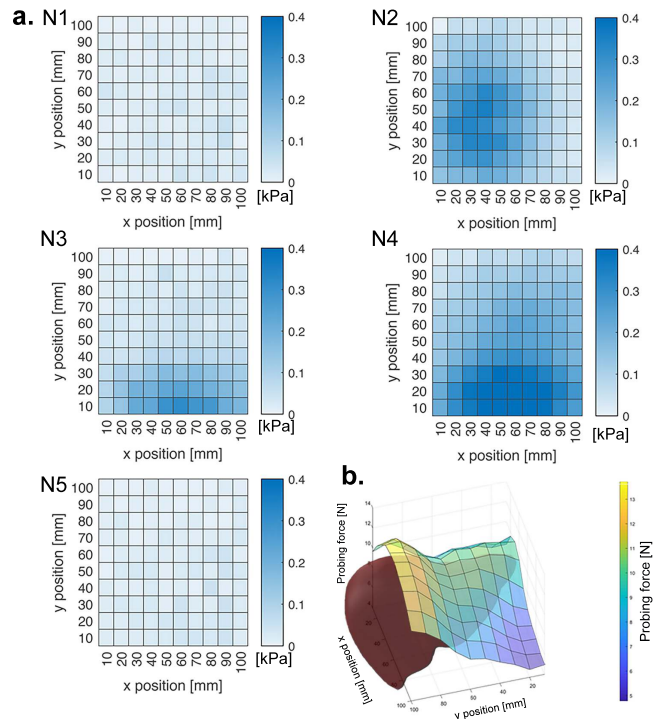

Fig. 13: **(a)** Maximum pressure change during the 20mm-depth indentation at different positions. x-axis and y-axis are the x and y position of the probe in regard to the phantom reference frame. The pressure change caused by the indentation is indicated by the color bar. Pressure change for nodule 1-5 is shown in N1-5, respectively. **(b)** 3D plot of the indentation force after the relaxation from the force/torque sensor during the indentation. The force map matches the shape of the liver because the organ is designed to be stiffer than the filling material in the phantom

Instrument DAQ (USB-6341) and Labview 2018. Fig. 11b shows the detailed connection of the set-up. The positions of the five nodules are shown in Figs. 11c and 11d. N2 and N4 are designed for left and right lobe lower surface fibrosis simulation. N1 and N3 are designed for left and right lobe edge fibrosis simulation. N5 is for the right lobe enlargement

simulation. Controller described in section III-C were used for controlling the internal driving pressure of the nodules.

To perform the point-by-point calibration, the phantom was palpated with repeated indentation by the probe on a grid of around 100×100 mm with the steps of 10 mm from the left top corner of the phantom to the right bottom corner. A clear correlation was observed between the indentation position and the reading from the pressure sensors, which supports the methodology and hypotheses stated previously. The reference frame and indentation region (the square with yellow lines) used in the calibration experiment are shown on Figs. 11c and 11d. The x and y positions of the indentations were controlled by the XY-stage. Within each trial of each point on the phantom, 4 random depth indentations were performed within the range of (5 to 30 mm depth) to acquire a wider range of force responses to generalize the model. Palpation force was kept within a similar range of manual palpation based on the previous study in [41]. Surface detection through the Force/Torque sensor was used to determine the indentation depth prior to the indentation. The pressure data (1000 Hz) of the embedded nodules and the force (100 Hz) and position (20 Hz) data of the probe were collected simultaneously for

calibration. The data were later being processed and resampled to 20 Hz for training purposes. In the experimental calibration, 6 combinations of selected driving pressure conditions of the nodules were tested (3 combinations were selected with extreme conditions where the driving pressure was either equal to the atmospheric pressure or the MCP of the nodule; 3 combinations were selected with randomly picked driving pressures in between). This 6 combinations of data formed the experimental training set.

The simulated training data were then computed based on the experimental training data and previously characterized sensing models (Fig. 10, Eq. (6) and (7)). The absolute sensitivity value is not being used here since it depends on the silicone thickness. However, the relative sensitivity curve of the driving pressure was assumed to remain the same. This method based on assumptions 1 and 2 was validated by comparing the measured pressure response of the phantom during indentations of randomly selected driving pressures to the simulated pressure response of the same driving pressure based on the sensing models and the experimental training data. The experimental data show a similar response to the simulated data with an average RMSE less than $0.02kPa$ across five trials of tests. This validates that the proposed methodology based on the assumptions can be used to generalize the model by supplementing the experimental training data with the simulated training data. A 0.2 N threshold has been applied on the training ground truth z-direction force data fz, where the xy-positions were set to be $(0,0)$ if the indentation force is less than the threshold. The pressure response from the nodules $\mathbf{P}$ was determined by: 1. the geometry, material, and nodule locations of the phantom, 2. the driving pressures of the nodules $\mathbf{N}$, 3. indentation force $\mathbf{f}$, and indentation position $\mathbf{u}$.

The experimental training set and simulated supplemental training were then shuffled to train a neural network model to estimate the hypothesis $\psi(\mathbf{P},\mathbf{N},\mathbf{u},\mathbf{f})$ for the pressure response, the driving pressure, the position, and the 3-axis force [43]. Multi-Layer Perceptron Neural Network (MLP) with Bayesian regularization function from MATLAB deep learning toolbox was used to fit the hypothesis with three hidden layers [7, 20, 8]. The data for the neural network training was formed as:

$$\mathbf{I}^{(i)} = \left[P_1^{(i)}\ P_2^{(i)}\ P_3^{(i)}\ P_4^{(i)}\ P_5^{(i)}\ N_1^{(i)}\ N_2^{(i)}\ N_3^{(i)}\ N_4^{(i)}\ N_5^{(i)} \right] \tag{8}$$

$$\mathbf{O}^{(i)} = \left[f_x^{(i)}\ f_y^{(i)}\ f_z^{(i)}\ x^{(i)}\ y^{(i)} \right] \tag{9}$$

where, $\mathbf{I}^{(i)}$ is the input vector of the neutral network, $P_1^{(i)}$ to $P_5^{(i)}$ are the pressure response of the nodule 1 to 5, $N_1^{(i)}$ to $N_5^{(i)}$ are the driving pressures of the nodule 1 to 5, $\mathbf{O}^{(i)}$ is the output vector of the neutral network, $f_x^{(i)}\ f_y^{(i)}$, and $f_z^{(i)}$ are the 3-axis indentation force, $x^{(i)}\ y^{(i)}$ are the indentation position. All positions are based on the phantom reference frame shown in Figs. 11c and 11d.

The performance of the trained neural network was then tested with a set of pressure data obtained by a new indentation experiment with randomly selected driving pressure combinations. The average estimation error for x position, y position, and z-direction force is 2.1 mm, 3 mm, and 0.55 N, respectively. The estimation with the generalized sensing model and the errors are shown in Figs. 12b-12d. x-direction force and y-direction force were used in the sensing model for generalization purposes. Only the z-direction force estimation error was evaluated and reported due to the small force applied in the other two axes. In Fig. 12d, the relaxation mainly comes from the viscoelastic behavior of the silicone. This can also be observed in palpation of soft tissue without any soft nodules [44]. A position estimation was also presented in Fig. 12 a, shows the ground truth indentation positions, estimated positions, and prediction errors in a 2D scale with regards to the phantom size and the calibrated indentation area on the top surface. Data are presented with only non-zero position estimations, and outliers have been removed based on the median value. The testing trial shows a root-mean-square error (RMSE) of 4 mm (in the testing area around 100×100 mm) and 1.18 N (for the applied force up to 18 N) for the position and force estimation of palpation, respectively.

B. Direct sensor reading from the nodule

Fig.13a shows the pressure change of the embedded soft nodules at each indentation position from nodule 1 to nodule 5 with a trial of 10×10 grid point-by-point indentation with the indentation depth of 20mm. The individual value shows the maximum pressure variations ($\Delta\mathbf{P} = \mathbf{P} - \mathbf{N}$) of the point-by-point palpation. Greater pressure variation indicates that the indentation applied greater pressure on the nodule. Fig. 13 also shows that the indentation from the top surface affects more on N2, N3, and N4 compared to N1 and N5. The simulated physical tumors embedded from distinctive regions of the liver would respond differently to the indentation. The presented pressure maps in Fig. 13 of the nodules can be used as one type of visual feedback to show the trainee which tumor on the liver experiences the highest pressure during the palpation.

To test the phantom with more complex palpation motions, rather than single-direction indentations, a robotic arm (UR5) with a sensorised probe (a capacitive tactile sensor adapted from [20], 2Hz sampling rate) was used to perform the palpation tasks. The capacitive tactile sensor has been calibrated to provide a force value. The validation set-up is shown in Fig. 14a. The palpation experiments were conducted through probing the abdominal phantom with a designed motion. Three types of motions were tested, as demonstrated in Figs. 14b-14d for palpation normal to the surface, palpation with lateral motion, and palpation with rotational motion. The sensor readings from the abdominal phantom and the sensor reading from the sensorised probe are both shown in Fig. 14e-14g. The palpation was performed on the same location on the phantom for the three types of demonstrated motions. A significant difference in the pressure reading profiles from the embedded nodules can be observed due to the different motions of palpation. The direct sensor readings from the phantom can, therefore, reflect the palpation motions and strategies. We also demonstrated this as one of the methods to present visual feedback simultaneously to the trainee.
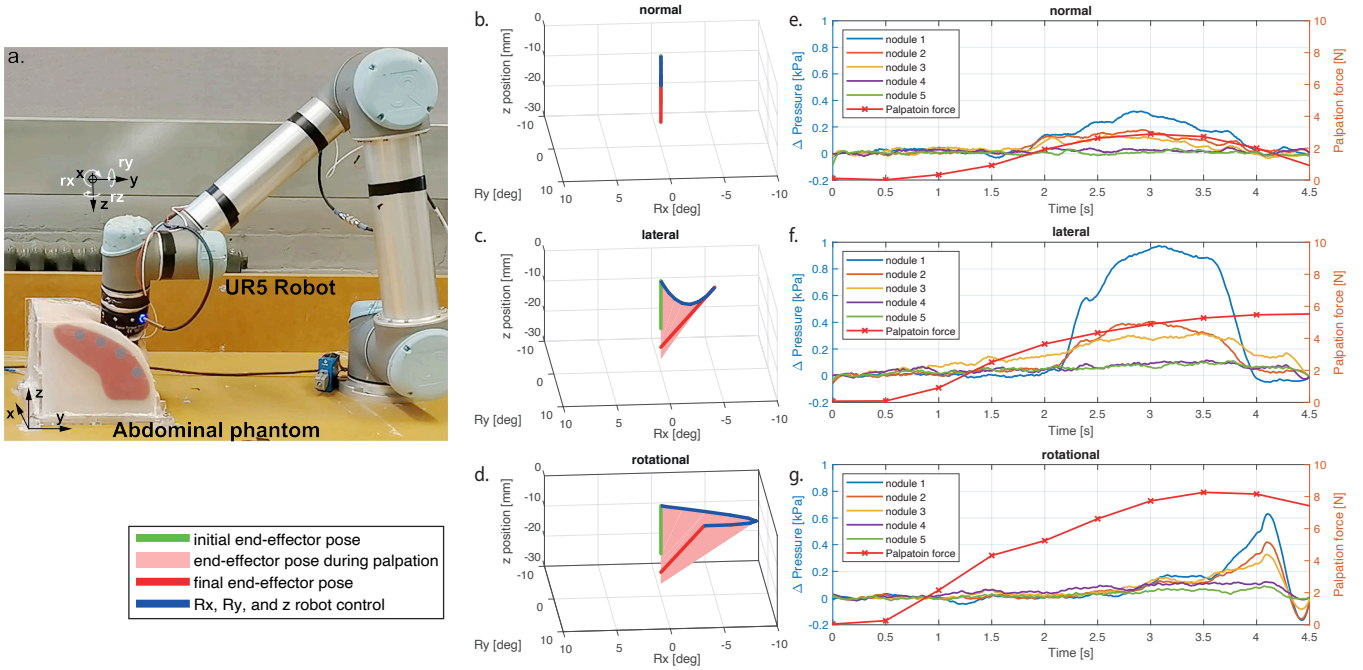
CONFIDENTIAL. Limited circulation. For review only
IEEE T-RO Submission no.: 20-0411.2

12

Fig. 14: **(a)** Validation set-up for palpation with complex motions performed with UR5 robot; **(b)** palpation trajectory with the motion normal to the surface; **(c)** palpation trajectory with the lateral motion; **(d)** palpation trajectory with the rotational motion. **(e), (f), (g)** Direct sensor reading from the phantom (5 embedded nodules) and force sensor reading from the probe with palpation with different motions performed at the same location.

C. Force and Position Estimation for Palpation with Complex Motions

A validation test was performed to test the position estimation accuracy of palpation with complex motions, through the set-up shown in Fig. 14a. Following the same methodology described in section V-A, a generalized neural network was trained based on the UR5 robot experimental training data and simulated training data. The driving pressures of the nodules are selected randomly for the test. The results show that the phantom can estimate the palpation position in regards to the palpation motions. Fig. 15 shows the result of the position estimation from a test trial palpation with normal, lateral, and rotational motions. The position estimation RMSE are 4.6mm, 6.2mm, and 2mm for normal, lateral, and rotational palpation, respectively.

Fig. 15: Position estimation with the trained sensing model for testing palpation with the normal, lateral, and rotational motion.

VI. DISCUSSION

Soft nodules with positive-pressurized cavities show a dual function of coupled actuation and sensing. The increased internal pressure can be used to control the stiffness of the nodule and dynamically simulate fibrosis in soft tissue. However, the nodule with only rubber membranes exhibits a very limited control region in pressure due to hyperelasticity. The nodule also shows inevitable significant deformation with the increase of stiffness during inflation. Experimental results denoted that the positive pressure granular jamming approach helps to extend the linear pressure-based control region of the material with a neo-Hookean assumption. It has the advantage of presenting a wide range of stiffness before the driving
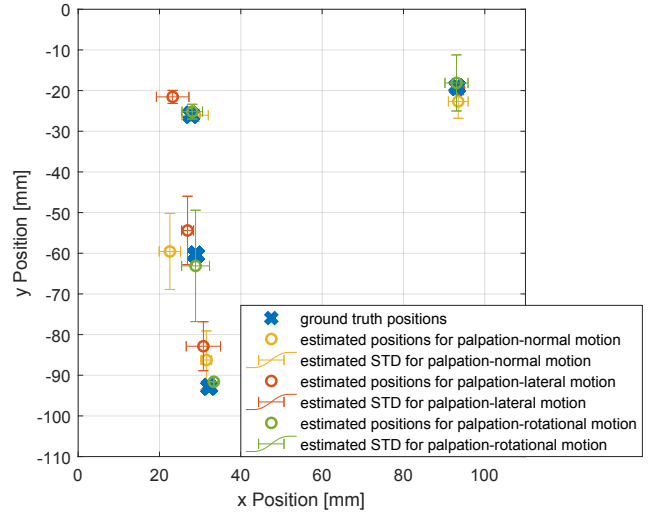
pressure saturated at its equilibrium state. The positive granular jamming layer can also be used to decouple the stiffness change and deformation by compensating the non-linearity of the elastomeric material. Thus, the design guideline for soft tumor physical simulation can be concluded as: 1) positive granular jamming nodules are suitable for applications where minimum size change is required for high range of stiffness simulation such as cirrhosis or hepatocellular carcinoma [34],

CONFIDENTIAL. Limited circulation. For review only
IEEE T-RO Submission no.: 20-0411.2

13

and 2) balloon nodules are suitable for applications where size changing is the major symptom, such as the enlarged liver..

The method introduced in Section V provides an effective solution to design soft robots with complex geometry and composite materials that can not only tune the stiffness distribution but also sense the interactions with multiple embedded nodules. This low-pressurized pneumatic solution poses great potential in the field of human-robot interaction with its advantages in safety, low-cost, high-flexibility, high-design freedom, and robustness. The technique can be used, but not limited to, the application of haptic surface, soft grippers, and soft sensorized simulators.

In this paper, we experimentally support its application in designing an abdominal phantom for the purpose of palpation training. Compared to existing soft sensing technologies used in haptic interaction such as sensing skins, the proposed concept: 1) introduces no interference to the physiological condition being presented by integrating pneumatic sensing and actuation, and 2) directly evaluates the effect of the tactile interaction on the organ by measuring pressure at the nodule level. These advantages allow a higher fidelity and more complex geometry of the simulator design. Together with the ability to present different stiffness and symptoms of the abnormal liver, the phantom can be used to train physicians to have a seamless transition to examine real patients using the same examination protocol. Organ level sensing also allows physicians to explore new external palpation techniques to detect organ conditions given force constraints imposed at the organ level. Compared to palpation training simulators that involve VR glasses and exoskeleton data gloves, the proposed concept requires no change to the existing manual palpation process with bare hands.

Through quantifying simulated conditions (tumor stiffness) and applied pressure on the simulated tumors, the proposed design can also provide a practical solution to understand the action and perception in haptic interaction. In future studies, systematic training solutions can be designed based on the abdominal phantom, allowing the trainees to record the technique, understand their behavior, and learn from expert demonstrations. We will also study the potential of multi-contact position estimation of the phantom via additional calibration and training of new neural networks.

VII. Conclusion

This paper characterized a coupled action-perception solution that will ultimately help to close the perception response loop in a robotic patient simulator to train physicians on how to regulate palpation forces and movements of fingers [1], [3]. However, this poses the challenge of being able to control the stiffness of the hard formations in soft tissue with internal pressure in a linear way without affecting the accuracy of sensing. To address this problem, we introduce a granular jamming approach to extend the linear region of the neo-Hookean behavior of pneumatically controlled soft actuators to present hard regions. Experimental results show the linear region of the neo-Hookean nodules can be extended by 140% with the positive pressure granular jamming approach compared to no-jamming conditions. Furthermore, by distributing the sensing

nodules in the abdominal tissue, soft sensing within complex 3D geometry can be achieved. Since the complex geometry and multi-material soft tissue have already incorporated non-linearity, keeping the single nodule sensing model within a linear range can significantly simplify the computation for generalizing the sensing model. Finally, we show results of estimating external palpation positions and forces even during driving pressures of the nodules (correspond to the simulated tumor conditions) not used to train the deep neural network used to generalize the model in Section V-A and Fig. 12. Testing trial with linear indentation palpation shows a root-mean-square error (RMSE) of 4 mm (in the testing area around 100×100 mm) and 1.18 N (for the applied force up to 18 N) for the position and force estimation of palpation, respectively. The position estimation RMSE of the complex palpation testing trial is 4.6mm, 6.2mm, and 2mm for normal, lateral, and rotational palpation in the same testing area, respectively. The accuracy is adequate for applications within the current study.

REFERENCES

[1] L. Bickley and P. Szilagyi, *Bates' guide to physical examination and history-taking*, 12th ed. Philadelphia : Wolters Kluwer, 2012, vol. 13.

[2] S. Ramani, "Twelve tips for excellent physical examination teaching," *Medical Teacher*, vol. 30, no. 9-10, pp. 851–856, 2008.

[3] C. Jarvis, *Physical examination & health assessment*, 7th ed. Elsevier B.V., 2015.

[4] C. L. Moore and J. A. Copel, "Point-of-care ultrasonography," *New England Journal of Medicine*, vol. 364, no. 8, pp. 749–757, 2011, pMID: 21345104.

[5] J. B. Cooper and V. R. Taqueti, "A brief history of the development of mannequin simulators for clinical education and training," *Quality and Safety in Health Care*, vol. 13, no. SUPPL. 1, pp. 11–18, 2004.

[6] G. Burdea, G. Patounakis, V. Popescu, and R. E. Weiss, "Virtual reality training for the diagnosis of prostate cancer," *Ieee 1998 Virtual Reality Annual International Symposium, Proceedings*, vol. 46, no. 10, pp. 190–197, 1998.

[7] G. J. Gerling, S. Rigsbee, R. M. Childress, and M. L. Martin, "The design and evaluation of a computerized and physical simulator for training clinical prostate exams," *IEEE Transactions on Systems, Man, and Cybernetics Part A:Systems and Humans*, vol. 39, no. 2, pp. 388–403, 2009.

[8] G. J. Gerling, A. M. Weissman, G. W. Thomas, and E. L. Dove, "Effectiveness of a dynamic breast examination training model to improve clinical breast examination (CBE) skills," *Cancer Detection and Prevention*, vol. 27, no. 6, pp. 451–456, 2003.

[9] A. Filippeschi, F. Brizzi, E. Ruffaldi, J. M. Jacinto, and C. A. Avizzano, "Encountered-type haptic interface for virtual interaction with real objects based on implicit surface haptic rendering for remote palpation," *IEEE International Conference on Intelligent Robots and Systems*, vol. 2015-Decem, pp. 5904–5909, 2015.

[10] J. Spillmann, S. Tuchschmid, and M. Harders, "Adaptive space warping to enhance passive haptics in an arthroscopy surgical simulator," *IEEE Transactions on Visualization and Computer Graphics*, vol. 19, no. 4, pp. 626–633, 2013.

[11] L. Hyde, C. Erolin, and J. Ker, "Creation of abdominal palpation model prototype for training of medical students in detection and diagnosis of liver disease," *Journal of Visual Communication in Medicine*, vol. 35, no. 3, pp. 104–114, 2012.

[12] K. Inoue, K. Ujiie, and S. Lee, "Development of haptic devices using flexible sheets for virtual training of abdominal palpation," *Advanced Robotics*, 2014.

CONFIDENTIAL. Limited circulation. For review only
IEEE T-RO Submission no.: 20-0411.2

14

[13] X. Tan, L. He, J. Cao, W. Chen, and T. Nanayakkara, "A soft pressure sensor skin for hand and wrist orthoses," *IEEE Robotics and Automation Letters*, vol. 5, no. 2, pp. 2192–2199, 2020.

[14] A. A. Stanley and A. M. Okamura, "Controllable Surface Haptics via Particle Jamming and Pneumatics," *IEEE Transactions on Haptics*, vol. 8, no. 1, pp. 20–30, 2015.

[15] Y. J. Kim, S. Cheng, S. Kim, and K. Iagnemma, "A novel layer jamming mechanism with tunable stiffness capability for minimally invasive surgery," *IEEE Transactions on Robotics*, vol. 29, no. 4, pp. 1031–1042, 2013.

[16] G. A. Dominguez, A. Schmitz, M. Kamezaki, and S. Sugano, "A Haptic interface with adjustable stiffness using MR fluid sophon somlor," *IEEE/ASME International Conference on Advanced Intelligent Mechatronics, AIM*, vol. 2015-August, pp. 1132–1137, 2015.

[17] M. J. Telleria, M. Hansen, D. Campbell, A. Servi, and M. L. Culpepper, "Modeling and implementation of solder-activated joints for single-actuator, centimeter-scale robotic mechanisms," *Proceedings - IEEE International Conference on Robotics and Automation*, pp. 1681–1686, 2010.

[18] A. Tzemanaki, G. A. Al, C. Melhuish, and S. Dogramadzi, "Design of a Wearable Fingertip Haptic Device for Remote Palpation: Characterisation and Interface with a Virtual Environment," *Frontiers in Robotics and AI*, vol. 5, no. June, pp. 1–15, 2018.

[19] L. He, Q. Lu, S.-A. Abad, N. Rojas, and T. Nanayakkara, "Soft fingertips with tactile sensing and active deformation for robust grasping of delicate objects," *IEEE Robotics and Automation Letters*, vol. 5, no. 2, pp. 2714–2721, 2020.

[20] P. Maiolino, M. Maggiali, G. Cannata, G. Metta, and L. Natale, "A flexible and robust large scale capacitive tactile system for robots," *IEEE Sensors Journal*, vol. 13, no. 10, pp. 3910–3917, 2013.

[21] L. Seminara, L. Pinna, M. Valle, L. Basiric, A. Loi, P. Cosseddu, A. Bonfiglio, A. Ascia, M. Biso, A. Ansaldo, D. Ricci, and G. Metta, "Piezoelectric polymer transducer arrays for flexible tactile sensors," *IEEE Sensors Journal*, vol. 13, no. 10, pp. 4022–4029, Oct 2013.

[22] S. Stassi, V. Cauda, G. Canavese, and C. F. Pirri, "Flexible tactile sensing based on piezoresistive composites: A review," *Sensors (Switzerland)*, vol. 14, no. 3, pp. 5296–5332, 2014.

[23] H. Zhao, K. O'Brien, S. Li, and R. F. Shepherd, "Optoelectronically innervated soft prosthetic hand via stretchable optical waveguides," *Science Robotics*, vol. 1, no. 1, 2016.

[24] M. Goka, H. Nakamoto, and S. Takenawa, "A magnetic type tactile sensor by gmr elements and inductors," in *2010 IEEE/RSJ International Conference on Intelligent Robots and Systems*, Oct 2010, pp. 885–890.

[25] T. Giffney, M. Xie, A. Yong, A. Wong, P. Mousset, A. McDaid, and K. Aw, "Soft Pneumatic Bending Actuator with Integrated Carbon Nanotube Displacement Sensor," *Robotics*, vol. 5, no. 1, p. 7, 2016.

[26] Y. L. Park, B. R. Chen, and R. J. Wood, "Design and fabrication of soft artificial skin using embedded microchannels and liquid conductors," *IEEE Sensors Journal*, vol. 12, no. 8, pp. 2711–2718, 2012.

[27] J. Hughes and F. Iida, "Tactile Sensing Applied to the Universal Gripper Using Conductive Thermoplastic Elastomer," *Soft Robotics*, vol. 5, no. 5, pp. 512–526, 2018.

[28] H. Yang, Y. Chen, Y. Sun, and L. Hao, "A novel pneumatic soft sensor for measuring contact force and curvature of a soft gripper," *Sensors and Actuators, A: Physical*, vol. 266, pp. 318–327, 2017.

[29] Y. Tanaka, K. Doumoto, A. Sano, and H. Fujimoto, "Development of a sensor system with syringe based on tactile sensing using balloon expansion," in *2010 IEEE International Conference on Robotics and Automation*, May 2010, pp. 4861–4866.

[30] L. He, N. Herzig, S. de Lusignan, and T. Nanayakkara, "Granular jamming based controllable organ design for abdominal palpation," in *2018 40th Annual International Conference of the IEEE Engineering in Medicine and Biology Society (EMBC)*, July 2018, pp. 2154–2157.

[31] A. Reuben, "Examination of the abdomen," *CLINICAL LIVER DISEASE*, vol. 7, no. 6, pp. 143–150, 2016.

[32] S. K. Venkatesh, M. Yin, J. F. Glockner, N. Takahashi, A. Philip, J. A. Talwalkar, and R. L. Ehman, "Magnetic Resonance Elastography of Liver Tumors- Preliminary Results," pp. 1534–1540, 2008.

[33] S. B. Edge, D. R. Byrd, C. C. Compton, A. G. Fritz, F. L. Greene, and A. Trotti III, "7th ed 2010 AJCC Cancer Staging Manual Seventh Edition," pp. 21–57, 2010.

[34] R. Masuzaki, R. Tateishi, H. Yoshida, T. Sato, T. Ohki, T. Goto, H. Yoshida, S. Sato, Y. Sugioka, H. Ikeda, S. Shiina, T. Kawabe, and M. Omata, "Assessing liver tumor stiffness by transient elastography.pdf," *Hepatology international*, vol. 1, no. 3, 2007.

[35] A. Shiva, S. H. Sadati, Y. Noh, J. Fra, A. Ataka, H. Wrdemann, H. Hauser, I. D. Walker, T. Nanayakkara, and K. Althoefer, "Elasticity

versus hyperelasticity considerations in quasistatic modeling of a soft finger-like robotic appendage for real-time position and force estimation," *Soft Robotics*, vol. 6, no. 2, pp. 228–249, 2019, pMID: 30702390.

[36] R. W. Ogden, "Large deformation isotropic elasticity–on the correlation of theory and experiment for incompressible rubberlike solids," *Proceedings of the Royal Society of London. A. Mathematical and Physical Sciences*, vol. 326, no. 1567, pp. 565–584, 1972.

[37] A. G. Holzapfel, "Nonlinear solid mechanics ii," 2000.

[38] N. G. Cheng, "Design and analysis of jammable granular systems," Ph.D. dissertation, Massachusetts Institute of Technology, 2013.

[39] L. Mullins, "Softening of rubber by deformation," *Rubber Chemistry and Technology*, vol. 42, no. 1, pp. 339–362, 1969.

[40] R. Jiusheng, "Elastic instability of pseudo-elastic rubber balloons," *Computers, Materials and Continua*, vol. 7, pp. 25–31, 02 2008.

[41] J. Konstantinova, G. Cotugno, P. Dasgupta, K. Althoefer, and T. Nanayakkara, "Palpation force modulation strategies to identify hard regions in soft tissue organs," *PLoS ONE*, 2017.

[42] L. Ljung, *System identification : theory for the user*, 2nd ed., ser. Prentice Hall information and system science series. Upper Saddle River, N.J. ; London: Prentice Hall, 1998.

[43] T. G. Thuruthel, B. Shih, C. Laschi, and M. T. Tolley, "Soft robot perception using embedded soft sensors and recurrent neural networks," *Science Robotics*, vol. 1488, p. accepted, 2018.

[44] N. Sornkarn, P. Dasgupta, and T. Nanayakkara, "Morphological computation of haptic perception of a controllable stiffness probe," *PLoS ONE*, 2016.